Journal of Catalysis 259 (2008) 211–222

Contents lists available at ScienceDirect

Journal of Catalysis

www.elsevier.com/locate/jcat

Steam and dry reforming of methane on Rh: Microkinetic analysis and hierarchy of kinetic models

Matteo Maestri [a,b], Dionisios G. Vlachos [a,*], Alessandra Beretta [b], Gianpiero Groppi [b], Enrico Tronconi [b]

[a] Department of Chemical Engineering and Center for Catalytic Science and Technology (CCST), University of Delaware-Newark, DE 19716-3110, USA
[b] Laboratory of Catalysis and Catalytic Processes, Dipartimento di Energia, Politecnico di Milano, Piazza Leonardo da Vinci 32, 20133 Milano, Italy

ARTICLE INFO

Article history:
Received 6 June 2008
Revised 2 August 2008
Accepted 16 August 2008
Available online 25 September 2008

Keywords:
Methane
Reforming
Water–gas shift reaction
Microkinetic model
Rhodium

ABSTRACT

CH_4 steam reforming (SR) and dry reforming (DR) on Rh have been analyzed using a comprehensive, thermodynamically consistent microkinetic model. Our analysis pointed out mechanistic analogies between the two processes. In particular, regardless of the co-reactant, methane consumption proceeds via pyrolysis and carbon oxidation by OH* ($CH_4 \rightarrow C^* \rightarrow CO^*$), and the role of the co-reactant (either CO_2 or H_2O) is to provide the main oxidizer, OH*. Moreover, in line with isotopic kinetic experiments reported in the literature, methane activation is predicted to be the rate-determining step, and all of the steps involving co-reactant turn out to be quasi-equilibrated. It also was found that under typical experimental conditions, SR and DR always occur with water–gas shift (WGS) reaction close to equilibrium. Adopting a systematic reduction methodology, we propose a hierarchy of models for SR and DR. In particular, first a reduced microkinetic model and then overall rate equations for the SR, DR, and WGS reactions are derived from the microkinetic models. Overall, our kinetic analysis is able to predict correctly the most important features found in experiments, namely that the overall reaction rate exhibits a first-order dependence on CH_4 concentration and is independent of the co-reactant (H_2O or CO_2). Product inhibition, which becomes important at lower temperatures, also is predicted.

1. Introduction

The possibility of a hydrogen economy [1,2] and the need for alternative clean fuels have renewed interest in hydrogen and especially in novel routes and/or sources for delocalized hydrogen production [3,4] as an alternative to the conventional steam reforming (SR) on Ni catalysts. The latter is an energy-intensive process (almost half of natural gas is burnt to supply the necessary heat), conducted at high pressure (15–30 atm) and characterized by a long residence time (1 s) [5]. Consequently, steam reformers on Ni are too bulky for use in decentralized, small-scale H_2 production [6] and must be replaced with processes that can occur at short contact times. Rh is a very good catalyst for CH_4 SR, dry reforming (DR), and partial oxidation (POX) of methane with excellent conversion and selectivity to syngas at very short contact times [7–9]; that is, the conventional bulky reformers could be replaced by about 100- to 1000-fold smaller reactors running on Rh. This attribute makes SR, DR, and POX on Rh possible solutions for distributed production of H_2 from natural gas.

Modeling of reforming reactors on Rh requires, among other things, reliable kinetic models, validated in an operating range relevant to practical applications. Understanding of the catalytic process at a fundamental level aids optimization of the process and the catalysts. In this respect, a comprehensive microkinetic model is an important tool for consolidating fundamental information about a catalytic process under different operating conditions [10,11]. Different from the semiempirical approaches, microkinetic modeling not only affords an analysis of the performance of catalytic reactors—in principle, valid over a wide range of operating conditions—but also offers fundamental insights into the reaction mechanism, leading, in conjunction with experimental information, to a deeper understanding of the catalytic process. In fact, it can elucidate the predominant paths, the rate-determining step (RDS) and the most abundant reactive intermediates (MARI) without *a priori* assumptions on elementary steps. It is an essential tool when fundamental aspects, such as the possible interaction between the surface and gas-phase chemistry, must be quantified [12]. But its implementation is often a demanding task in terms of CPU time, especially when fast model responses are required (e.g., for online process control and computational fluid dynamics [CFD] simulations) or fundamental information about the catalytic process is not needed. In those cases, overall rate expressions are often preferred. Thus, it is apparent that a hierarchy of kinetic models is called for in reactor modeling [13,14].

Several kinetic models for reforming and partial oxidation of CH_4 on Rh catalysts, both detailed [15–17] and molecular [18–20],

* Corresponding author. Fax: +1 302 831 1048.
E-mail address: vlachos@udel.edu (D.G. Vlachos).

0021-9517/$ – see front matter
doi:10.1016/j.jcat.2008.08.008

Table 1
Summary of key experimental findings for SR and DR

Author	Notes	Findings/comments	Proposed kinetic/mechanism
Wei and Iglesia [36]	*Catalyst:* Rh H_2O/CH_4 and CO_2/CH_4: 0.4 to 2 *Temperature*: 873 to 1023 K *Conversions*: lower than 5–10%	a) CH_4 activation is the only kinetically relevant step b) No kinetic effect of co-reactant (either H_2O or CO_2) c) WGS always occurs at equilibrium along with SR/DR d) No product inhibition on reaction rate e) SR and DR proceed with the same rate	a) Methane reacts via pyrolysis: $CH_4 \rightarrow C^* + 4H$ b) Methane pyrolysis is the RDS c) C^* oxidation by O^* d) Co-reactant steps assumed at equilibrium
Rostrup-Nielsen and Hansen [41]	*Catalyst:* Ni, Ru, Rh, Pd, Ir, Pt	a) SR and DR proceed with the same rate b) No kinetic effect of co-reactant (either H_2O or CO_2) c) WGS at equilibrium	a) Methane reacts via pyrolysis: $CH_4 \rightarrow C^* + 4H$ b) C^* oxidation by O^* c) RDS: CH_4 pyrolysis and C^* oxidation
Bradford and Vannice [38]	*Catalyst:* Ni CH_4–CO_2 mixtures *Temperature*: 673 to 823 K	a) CO_2 has a negligible effect on CH_4 conversion at ratios $CO_2/CH_4 \geqslant 1$ b) A negative reaction order in CO_2 for $CO_2/CH_4 \leqslant 1$ c) Reverse-WGS at equilibrium	a) Methane reacts via pyrolysis: $CH_x^* + * \rightarrow CH_{x-1}^* + H^*$ b) CH_x^* reacts with surface OH^* (from reverse WGS) to CH_xO c) CH_4 pyrolysis and CH_xO decomposition to CO are RDS
Donazzi et al. [18,23]	*Catalyst:* Rh H_2O/CH_4 and CO_2/CH_4: 1 to 4 *Temperature*: 300 to 850 K *Conversions*: up to 100%	a) 1st-order dependence on CH_4 b) No kinetic effect of H_2O in SR c) Kinetic effect of CO_2 in DR for $CO_2/CH_4 \leqslant 1$ d) SR and DR proceed with the same rate for co-reactant/$CH_4 > 1$ e) Product inhibition possible	a) DR is considered the summation of SR and reverse WGS b) For $CO_2/CH_4 > 1$, the reverse WGS is at equilibrium

have been reported, but in general they suffer from different limitations, including a limited range of validity or lack of thermodynamic consistency. We have recently proposed [21,22] a new version of the microkinetic model of Mhadeshwar and Vlachos [16], using a comprehensive experimental data set of various processes [18,23], according to a hierarchical multiscale methodology [16,21,22,24,25]. The activation energies are predicted using the unity bond index quadratic exponential potential (UBI-QEP) theory [26,27], and coverage effects are accounted for using DFT. Our single-site, mean field-based microkinetic model is able to predict quantitatively the effect of different feed compositions and temperature for various reacting systems, including SR ($CH_4 + H_2O$), DR ($CH_4 + CO_2$), POX ($CH_4 + O_2$), hydrogen ($H_2 + O_2$) and carbon monoxide ($CO + O_2$)-rich combustion, the water–gas shift (WGS; $CO + H_2O$), and the reverse water–gas shift (RWGS; $CO_2 + H_2$).

In this work, we present a detailed analysis of the catalytic mechanism of SR and DR processes to rationalize the experimental data and trends. Then we derive a hierarchy of models for CH_4–H_2O and CH_4–CO_2 reacting systems, ranging from a reduced microkinetic model to overall two-step rate expressions for SR and DR. In contrast to the classical approaches, where overall expressions are usually based either on *ad hoc* power-law fitting or on an *assumed* reaction mechanism and RDS (e.g., Langmuir–Hinshelwood–Hougen–Watson [28]), we perform a top-down hierarchical model reduction, where the information of the higher-level model is exploited for the development of the lower-level model. In this way, no *a priori* assumptions are required at any step. In particular, the paper comprises two main sections. In the first section, we report a microkinetic analysis of CH_4–H_2O and CH_4–CO_2 reacting systems using the full microkinetic model [21,22]. This analysis involves identification of the main elementary-like reaction paths, MARI and RDS, with no *a priori* assumption on reaction steps. In the second section, we propose a hierarchical chemistry reduction [29–31] of the full microkinetic model to derive a reduced microkinetic model for $CH_4/H_2O/CO_2$ reacting systems and two-step rate expressions. In doing so, the two-step rate expressions are not based on chemical hypotheses, and the effective parameters are not determined by regression of experimental data, but rather are directly related to the rate constants of the elementary-like reactions of the microkinetic model. Comparisons to experimental data and to the key experimental findings reported in the literature also are made. For the sake of clarity, a summary of such literature findings is reported in Table 1.

2. Full microkinetic model-based analysis

For the analysis, we used our C_1 single-site microkinetic model [21,22], under the assumption of thermal equilibrium between the catalyst particle and its environment and the mean-field approximation.

2.1. Comparison to experimental data

The SR and DR data of Donazzi et al. [23] in an annular reactor were simulated using a one-dimensional heterogeneous model [19,32]. This model was assessed in previous work. In addition, transport effects are not significant under most conditions. Model equations and reactor details are reported in Table 2. The measured experimental Rh dispersion and weight (5% and 10 mg of 4% Rh-Al_2O_3, respectively) were considered input in the simulations, giving rise to a Rh surface per unit reactor volume (a_v) of 600 cm^{-1}. Only this parameter should be input each time that the catalyst changes; the kinetic parameters remain the same. Fig. 1 compares predictions using the entire microkinetic model of 82 elementary-like reactions [21,22] to experimental data, in terms of CH_4 conversion. The full microkinetic model was able to predict both SR and DR experimental data reasonably well, except for the DR experiment with $CO_2/CH_4 = 1$, where the model overestimates the CH_4 conversion considerably (square symbols in Fig. 1b). Fig. 2 compares DR and SR at different temperatures (solid lines). The model correctly predicted the trend with temperature for both reactants and products.

2.2. Main reaction paths and rate-determining step

Here we present an analysis of the full microkinetic model for SR and DR on Rh [21,22], with the aim of identifying the main elementary-like reaction pathways, the RDS, and the main molecular stoichiometries. We refer our analysis to the experimental data reported in Fig. 2.

2.2.1. Steam reforming

To identify the main reaction pathways from reactants to products involved in SR, we carried out reaction path analysis (RPA), based on the net production rate of each surface species [33]. The analysis was performed at three selected temperatures (400, 500, and 600 °C), at which moderate to high conversions were observed (Fig. 2). Results are reported in Fig. 3a for 500 °C. Similar results were found for the other two temperatures investigated.

Table 2
Governing equations and reactor parameters

Model equations	
$\frac{dW_i}{dV} = k_{mat,i}\rho a_V(\omega_i^{wall} - \omega_i^{bulk})$,	(1)
$k_{mat,i}\rho a_V(\omega_i^{wall} - \omega_i^{bulk}) = \left(\sum_{j=1}^{NR}\nu_{i,j}r_j\right)a_{Rh}MW_i$,	(2)
$Sh_i = \frac{k_{mat,i}d_h}{D_i} = 5.21 + 6.874\exp(-71.2z_i^*)(1000z_i^*)^{-0.35}$,	(3)
where: $z_i^* = \frac{D_i z}{v d_h^2}$ (Ref. [32]),	
Reactor configuration and parameters	
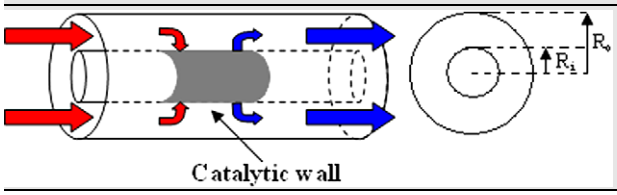	Annular reactor Inner radius (R_i): 0.2 cm Outer radius (R_o): 0.25 cm Reactor length: 2.2 cm

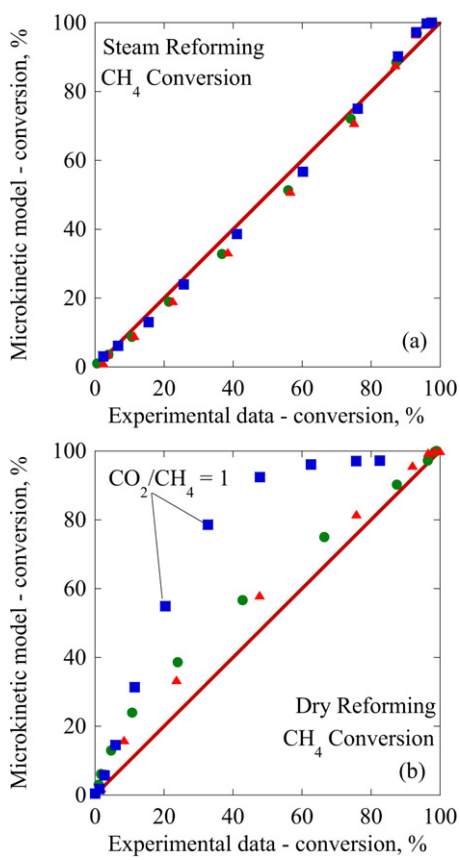

Fig. 1. Comparison between model results and experimental data for SR (a) and DR (b). SR: CH_4 1%–H_2O 1.5 to 2.5%. DR: CH_4 1%–CO_2 1 to 4%. Temperature range: from 300 to 850 °C. Details reported in Ref. [18,23].

Our model predicts that methane will adsorb dissociatively on Rh and dehydrogenate to C* (hereafter * implies an adsorbed species or a vacant site) via pyrolysis ($CH_4 + 5^* \rightarrow C^* + 4H^*$). OH*, provided via the adsorption and dissociation of water into OH* and H*, oxidizes C* to CO*, according to

$$C^* + OH^* \rightarrow CO^* + H^* \ (R_{79}).$$

Then CO* partly desorbs and is partially oxidized by OH* to CO_2^* mainly via a direct pathway ($CO^* + OH^* \rightarrow CO_2^* + H^*$, R_{29}). The path involving COOH* ($CO^* + OH^* \rightarrow COOH^* \rightarrow CO_2^* + H^*$, R_{32} and R_{33}) also is predicted to occur but to be considerably slower than the direct one (R_{29}), whereas the path involving HCOO* appears to be totally negligible under these conditions.

To identify which reaction steps are in quasi-equilibrium, the partial equilibrium (PE) ratio, φ (defined as $\varphi = \frac{r_f}{r_f + r_b}$) is reported in Fig. 4a for each reaction pair reported in the RPA. Here r_f and r_b are the forward and backward rates, respectively. Given its definition, a value of $\varphi = 0.5$ indicates that the reaction is in PE (i.e., $r_f = r_b$), whereas when φ deviates from 0.5, the reaction is not in PE ($\varphi = 1$ for $r_b = 0$; $\varphi = 0$ for $r_f = 0$).

Our results indicate that all of the steps involving OH* were quasi-equilibrated, and that in the CH_4 pyrolysis, all of the steps were at near equilibrium, except for the $CH_3^* + * \rightarrow CH_2^* + H^*$ step, which clearly is far from equilibrium. Thus, according to Dumesic's criterion [34], CH_3^* dehydrogenation turned out to be the RDS.

Fig. 5 shows the energetics of the CH_4 pyrolysis steps. Along the dehydrogenation path, the step with the highest activation energy was $CH^* + * \rightarrow C^* + H^*$. Thus, based on energetics, this step would be expected to be the limiting one. In contrast, the trend for the energetics of the hydrogenation path ($CH_{x-1}^* + H^* \rightarrow CH_x^* + *$) was the opposite; in particular, the $CH_2^* + H^*$ association turned out to have the highest activation energy. It follows that for intermediate and high temperatures, the CH_4, CH_2^*, and CH* steps quickly reached quasi-equilibrium, whereas CH_3^* decomposition was far from equilibrium, due to the high activation energy of the reverse reaction. Consequently, this step becomes the RDS.

We also evaluated the RDS through sensitivity analysis (SA). In particular, we performed SA on the exit molar fraction of CH_4, CO, CO_2, H_2, and H_2O, by perturbing the pre-exponentials of each reaction pair by 10% at the three temperatures. Results for the CH_4 outlet mole fraction, reported in Fig. 6, clearly show that the system was highly sensitive to the CH_3^* dehydrogenation step ($CH_3^* + * \rightarrow CH_2^* + H^*$). Qualitative similar results were obtained for CO, CO_2, H_2, and H_2O (data not shown). Thus, according both to Dumesic's [34] and SA criteria, the CH_3^* dehydrogenation step ($CH_3^* + * \rightarrow CH_2^* + H^*$) turned out to be the RDS.

2.2.2. Dry reforming

We performed the same analysis for DR. Fig. 3b shows the dominant reaction paths at 500 °C. As in SR, here CH_4 followed a pyrolytic path, giving rise to C* on the catalyst surface, which was oxidized by OH* to CO*. Different from SR, CO_2 adsorbed on the surface, and its activation was due to H*, according to

$$CO_2^* + H^* \rightarrow CO^* + OH^* \ (R_{29}).$$

The CO_2 decomposition path ($CO_2^* + * \rightarrow CO^* + O^*$, R_{23}), considered by some to be the main path for CO_2 activation [35,36],

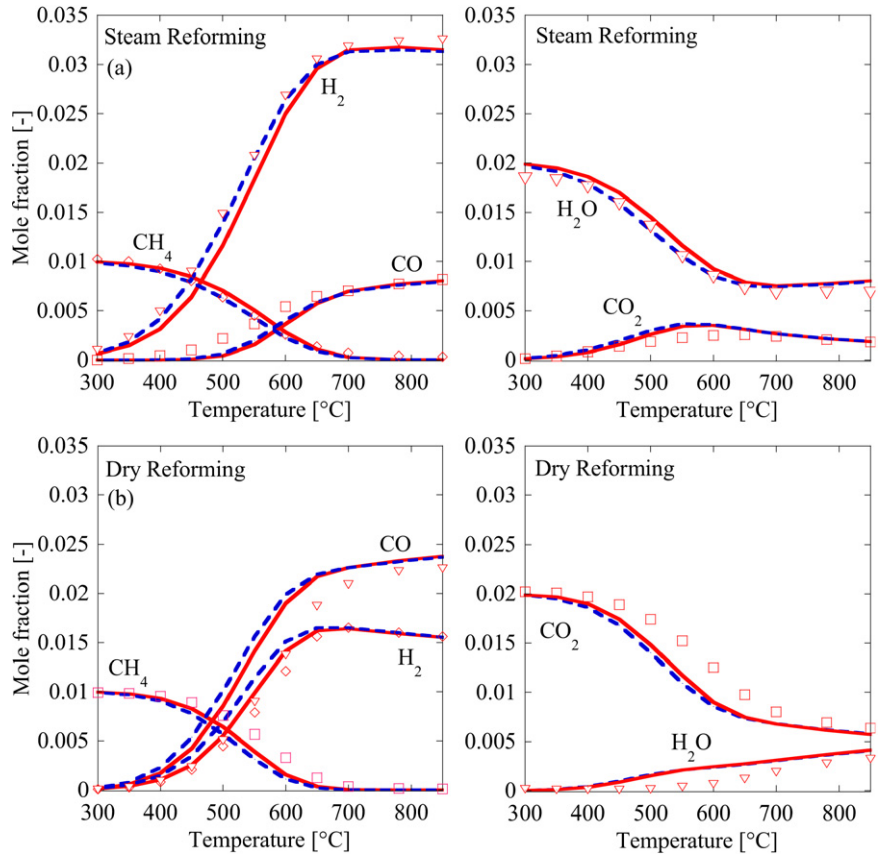

Fig. 2. Outlet mole fractions at different reactor temperatures. Solid lines: full microkinetic model. Dashed lines: 2-step reduced molecular model with fitted activation energies (Table 7). Symbols: experimental data of Donazzi et al. [18,23]. Panel (a) SR. Inlet conditions: molar composition of CH_4 0.01–H_2O 0.02–N_2 0.97; GHSV 2×10^6 Nl/kg/h; Panel (b) DR. Inlet conditions: molar composition of CH_4 0.01–CO_2 0.02–N_2 0.97; GHSV 2×10^6 Nl/kg/h.

occurring parallel to R_{29}, was found to be negligible at the conditions used in the present investigation, in line with previously reported infrared and kinetic measurements [37]. Consequently, the oxidizer OH* in R_{79} was produced not via oxidation of H* by O* (with O* formed in turn from CO_2 decomposition), but directly from R_{29}. Moreover, part of the OH* reacted with H*, giving rise to H_2O^*, as was also found experimentally. As in SR, in DR the steps involving the co-reactant turned out to be quasi-equilibrated (Fig. 3b) and PE analysis and SA identified the CH_3^* dehydrogenation step ($CH_3^* + * \rightarrow CH_2^* + H^*$) as the RDS.

An analysis of the reaction paths and RDS raises analogies between the two processes. In particular, regardless of the co-reactant, methane consumption ($CH_4 \rightarrow C^* \rightarrow CO^*$) occurs via pyrolysis, and carbon oxidation occurs via OH*. A key observation is that, according to our model, the main oxidizer turned out to be OH* and not O*, different from most qualitative mechanisms reported in the literature [35–37], which usually assume that the main oxidizer is O*, coming from $OH^* + * \rightarrow H^* + O^*$ for SR and from $CO_2^* + * \rightarrow CO^* + O^*$ for DR. According to our calculations, those pathways (both of which are accounted for in the full microkinetic model) do not occur, because parallel consumption paths (R_{79} and R_{29}, respectively) turn out to be favored at the investigated conditions.

In both systems, the role of the co-reactant (either CO_2 or H_2O) is to provide the OH* needed for C* oxidation and, in line with the isotopic experiments of [36], all of the steps involving OH* turn out to be quasi-equilibrated. Moreover, because the RDS is independent of OH*, the co-reactant is not expected to play any kinetically relevant role in the reaction rate, if all of the steps involving OH* remain quasi-equilibrated. We verified this hypothesis by performing simulations of SR and DR at fixed CH_4 mole fraction and different inlet fractions of the co-reactant. The results are reported in Fig. 7. In this respect, our model results are in agreement with the experimental evidence reported in the literature (see Table 1). Regarding the role of CO_2 in DR (for CO_2/CH_4 ratios $\leqslant 1$), there is no general consensus among experiments. In particular, Wei and Iglesia [36] found an independence of CO_2, whereas Donazzi et al. [18,23] and Bradford and Vannice [38] observed an effect of CO_2 on the reaction rate. Our kinetic model is in line with the observations of Wei and Iglesia, because the steps involving CO_2 remain quasi-equilibrated even at CO_2/CH_4 ratios. This leads to considerable overestimation of the methane conversion with respect to the experimental data [18,23] for a CO_2/CH_4 ratio to 1 (square symbols in Fig. 1b). A previous study [23] suggested that for $CO_2/CH_4 \leqslant 1$, CO_2 activation (i.e., the RWGS) becomes the RDS. This change in RDS could be related to additional phenomena not accounted for in our model, such as carbon deposition leading to some catalyst deactivation, which possibly could occur under oxidant lean conditions. Thus, the model is not recommended for low CO_2/CH_4 ratios.

Later in the paper, we report an analysis of the reaction orders of reactants and products on the overall reaction rates.

2.3. Most abundant reactive intermediates (MARI)

Fig. 8 shows the MARI for SR and DR at 400 and 600 °C. CO* and H* are the MARI for both processes, but the surface coverages are different. In particular, in DR the coverage of CO* changes considerably (from 0.5 to 0.2 as the temperature increases from 400 to 600 °C), whereas in SR the coverages of CO* and H* do not vary much with temperature.

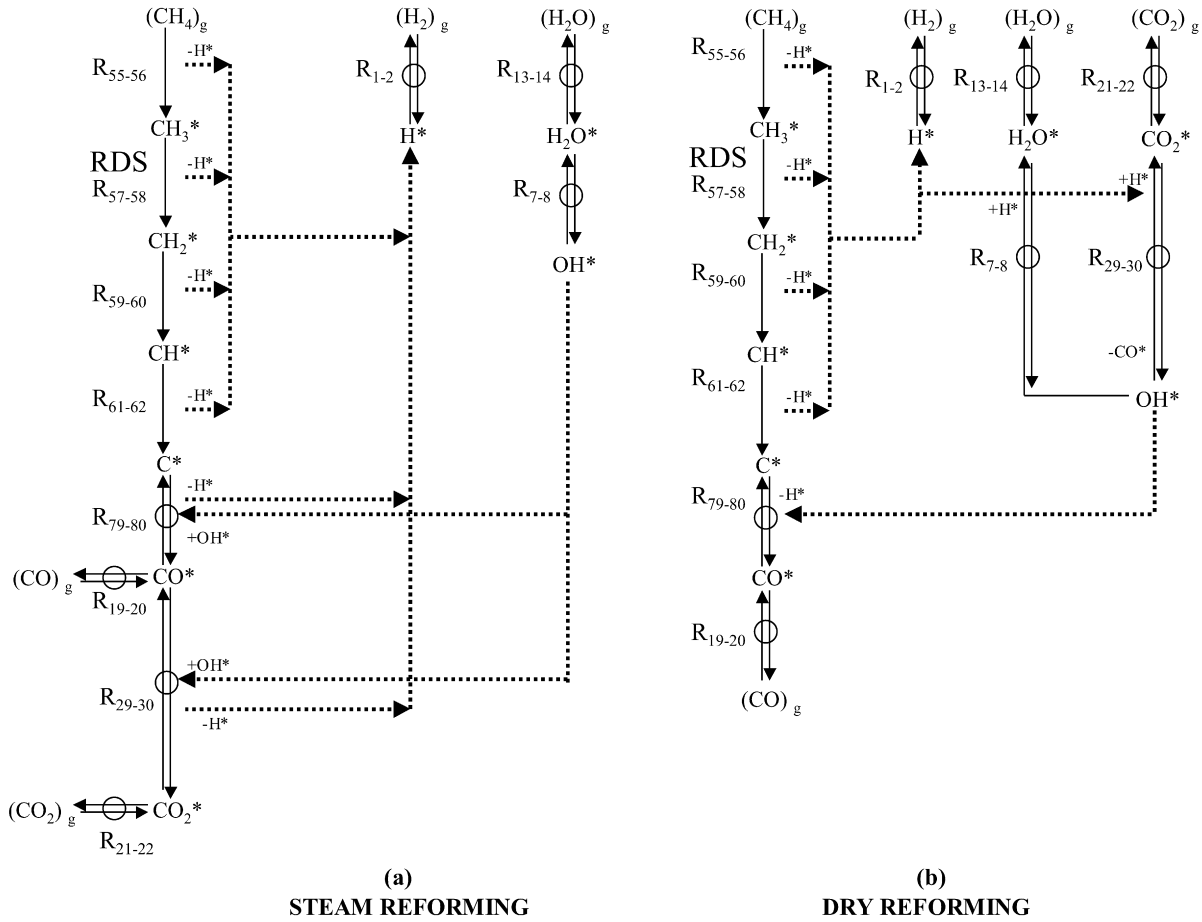

Fig. 3. Reaction path analysis at reactor outlet at 500 °C for (a) SR and (b) DR. The conditions are those of Fig. 2.

Although the kinetic equivalence in reaction paths of SR and DR is apparent, quantitative equivalence of SR and DR rates also depends on surface coverages, due to the coverage dependence of the reaction rate constants. Nonetheless, for temperatures above 600 °C, the surface turns out to be reasonably clean (free Rh sites >70%), and thus the coverage dependence of the energetics becomes negligible. At very low temperatures, on the other hand, little inhibition occurs due to low conversions. As a result, superposition of the conversion data of Fig. 7 (not shown) shows that even at lower temperatures, despite the different coverages, there are minor differences between the rates of the two processes, in agreement with the experimental evidence.

2.4. Overall molecular stoichiometries

The RPA reported in Fig. 3 indicates two overall molecular paths in the flow from reactants to products. In SR, CH_4 and H_2O convert to CO and H_2, and then CO reacts with H_2O, leading to CO_2 and H_2. In DR, CH_4 and CO_2 convert to CO and H_2, and CO_2 and H_2 produce H_2O and CO. The global stoichiometries of the overall molecular paths are

$$CH_4 + H_2O \rightleftharpoons CO + 3H_2 \qquad \text{(SR)}$$

or

$$CH_4 + CO_2 \rightleftharpoons 2CO + 2H_2 \qquad \text{(DR)}$$

along with

$$CO + H_2O \rightleftharpoons CO_2 + H_2. \qquad \text{(WGS)}$$

These overall stoichiometries can be confirmed by computing the rates of reactants and products at reactor location and extracting the relative ratios, as suggested previously [31].

3. Hierarchical modeling

In this section, we present a hierarchical chemistry reduction of the full microkinetic model. First, a reduced microkinetic model for $CH_4/H_2O/CO_2$ reacting systems is presented, discarding all of the elementary-like steps that play no role. Then we derive overall rate equations for the three molecular pathways, exploiting information obtained with microkinetic analysis that forms the basis for making a posteriori assumptions for model reduction.

3.1. Reduced microkinetic model for SR and DR

As expected, not all of the paths included in the microkinetic model are important, but different compositions and operating conditions may activate different paths. It follows that out of the 41 reversible reactions included in the full microkinetic model for CH_4 POX [21,22], only some are needed to model SR and DR data. To identify the elementary-like steps that may play a role in the SR/DR reacting system, we performed principal component analysis (PCA), using the information from the SA at three temperatures [39,40]. In PCA, we considered the matrix S, where $S_{i,j}$ is the sensitivity coefficient of the mole fraction of the ith species at the reactor outlet with respect to the jth reversible reaction. In particular, we performed SA on the outlet mole fraction of CH_4, CO, CO_2, H_2, and H_2O, for both SR ($CH_4 = H_2O = 1\%$) and DR ($CH_4 = CO_2 = 1\%$). In summary, we considered 30 sensitivity coefficients

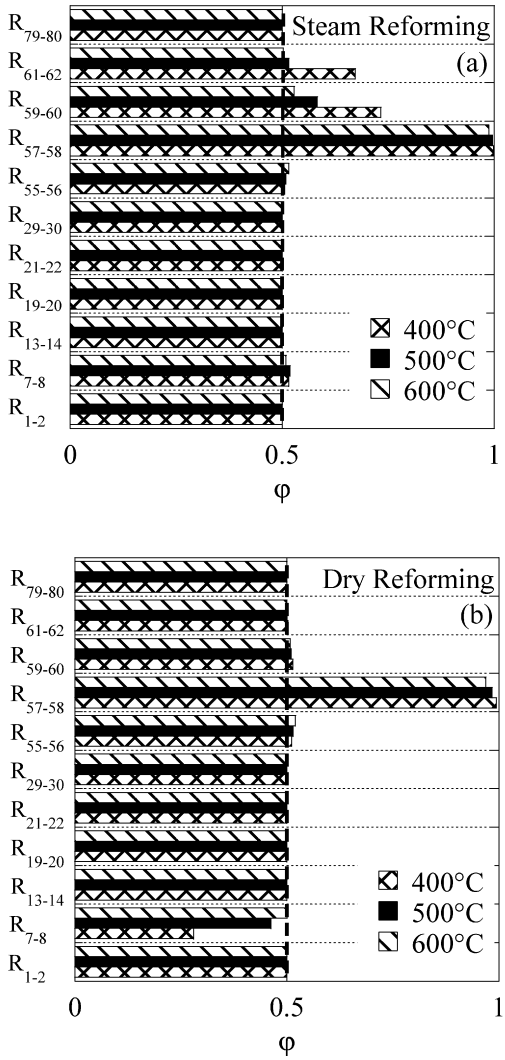

Fig. 4. Partial equilibrium ratio at three temperatures indicated for (a) SR and (b) DR. The conditions are those of Fig. 2.

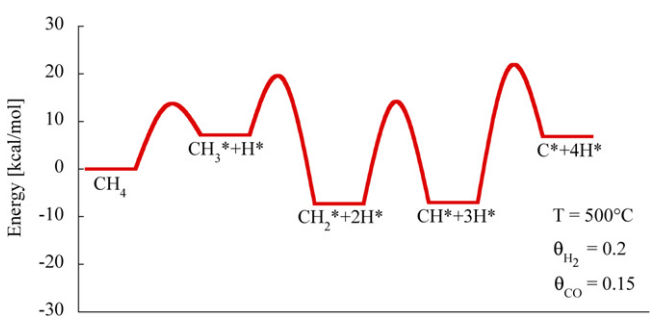

Fig. 5. Activation energies for CH_x decomposition according to the UBI-QEP theory [26] at 500 °C and for $\theta_H = 0.2$ and $\theta_{CO} = 0.15$. Details are reported elsewhere [21,22]. For CH_4, dissociative adsorption has been considered.

(5 species at 3 temperatures for SR and DR). Because the full mechanism consists of 41 reversible reactions, the dimension of the matrix S is 41 × 30, and the matrix SS^T is a square 41 × 41 matrix with 41 eigenvalues. Table 3 reports the first three eigenvalues along with their eigenvectors. There is a considerable disparity between the eigenvalues; in particular, only one turns out to be very important (3rd and 6th columns of numbers in Table 3). Considering a threshold value of 10^{-5} for the elements of the eigenvectors for the top three eigenvalues, from the 41 reversible reactions of the full mechanism, a reduced mechanism of 19 reversible reac-

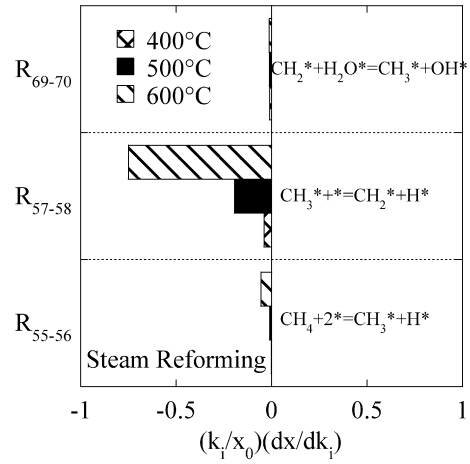

Fig. 6. Sensitivity of CH_4 mole fraction with respect to pre-exponentials at three temperatures for SR. Inlet composition of CH_4 0.01–H_2O 0.02 (balance N_2; other conditions as in Fig. 2). Only the most sensitive reaction pairs are reported.

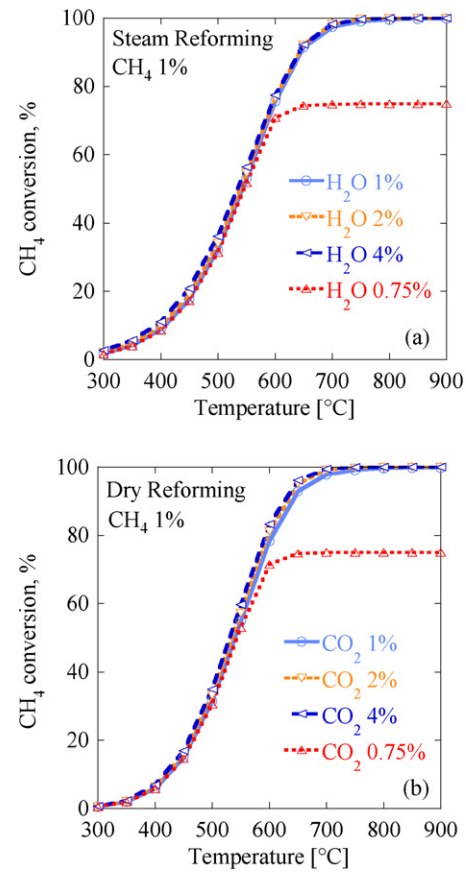

Fig. 7. CH_4 conversion at different inlet mole fractions of co-reactant for (a) SR and (b) DR. Other conditions as in Fig. 2.

tions was obtained. This threshold was chosen to include all the adsorption/desorption steps of the molecular species involved in the process in the reduced, elementary-like model. The reduced microkinetic model is reported in Table 4. The predictions of the two microkinetic models were compared under different operating conditions, and no differences between the two models were found (results not shown).

3.2. A two-step reaction mechanism

Here, using the information obtained with the microkinetic analysis, we attempt to derive overall rate expressions for SR, DR,

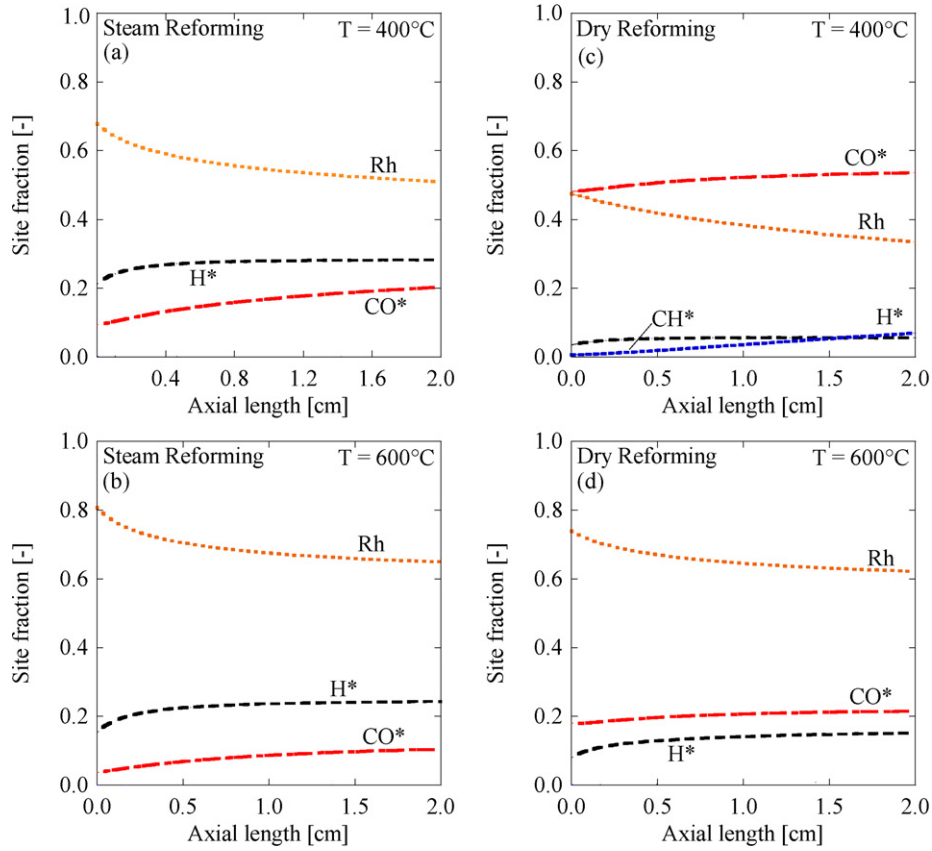

Fig. 8. Dominant surface coverages as a function of reactor length for SR (panels (a) and (b)) and DR (panels (c) and (d)). Other conditions as in Fig. 2.

Table 3
Principal component analysis of methane steam and dry reforming on a Rh/alumina catalyst

Eigenvalues	0.0053	0.73	7.81	Eigenvalues	0.0053	0.73	7.81
Reaction	Eigenvector	Eigenvector	Eigenvector	Reaction	Eigenvector	Eigenvector	Eigenvector
R_{1-2}	**2.88E-04**	**−6.36E-05**	−7.83E-06	R_{43-44}	−3.59E-07	−1.90E-07	−2.23E-08
R_{3-4}	−2.26E-07	−2.82E-09	2.73E-09	R_{45-46}	−3.77E-07	−1.03E-07	1.78E-08
R_{5-6}	−8.41E-07	−3.51E-07	2.86E-08	R_{47-48}	0.00E+00	0.00E+00	0.00E+00
R_{7-8}	**8.47E-03**	**9.91E-01**	**1.31E-01**	R_{49-50}	−8.16E-07	−2.76E-07	2.39E-08
R_{9-10}	**1.00E-01**	**6.79E-03**	**4.97E-03**	R_{51-52}	−2.44E-07	−1.39E-07	6.73E-09
R_{11-12}	−2.40E-07	−7.87E-09	9.80E-09	R_{53-54}	−1.47E-07	1.31E-08	−4.96E-10
R_{13-14}	**−5.05E-04**	**8.72E-05**	**3.16E-05**	**R_{55-56}**	**9.94E-01**	**−3.59E-03**	**−4.35E-02**
R_{15-16}	1.43E-06	−1.22E-07	−7.31E-08	**R_{57-58}**	**−4.20E-02**	**1.31E-01**	**−9.90E-01**
R_{17-18}	−1.22E-07	−1.63E-09	1.47E-09	**R_{59-60}**	**5.01E-03**	**1.36E-03**	**−5.61E-04**
R_{19-20}	**−1.49E-03**	**1.35E-03**	**−2.44E-04**	**R_{61-62}**	**2.01E-04**	**3.36E-03**	**−8.97E-04**
R_{21-22}	**−9.49E-04**	**6.85E-04**	**4.95E-04**	**R_{63-64}**	**−2.29E-04**	**3.30E-05**	**−1.14E-04**
R_{23-24}	−2.80E-07	−7.16E-08	7.42E-09	R_{65-66}	−1.18E-06	−3.41E-07	6.82E-09
R_{25-26}	3.81E-07	−8.16E-10	9.45E-09	R_{67-68}	−3.18E-06	−2.52E-07	6.24E-08
R_{27-28}	−9.24E-08	−1.24E-09	1.12E-09	**R_{69-70}**	**−3.05E-03**	**4.14E-04**	**−1.99E-04**
R_{29-30}	**−1.30E-03**	**2.26E-04**	**6.22E-05**	**R_{71-72}**	**−2.40E-05**	**1.77E-05**	−6.26E-07
R_{31-32}	**−1.56E-05**	−2.75E-07	5.45E-08	**R_{73-74}**	**−1.74E-04**	**3.10E-04**	6.93E-06
R_{33-34}	**1.04E-05**	−6.00E-06	9.91E-07	R_{75-76}	−5.46E-07	−2.73E-08	−1.10E-08
R_{35-36}	**1.35E-04**	**3.45E-04**	**1.34E-05**	R_{77-78}	−6.27E-08	−6.65E-08	1.53E-08
R_{37-38}	−4.62E-07	−1.20E-07	1.14E-08	**R_{79-80}**	**1.39E-03**	**7.32E-05**	**−2.05E-05**
R_{39-40}	**1.71E-04**	**2.01E-04**	6.91E-06	R_{81-82}	3.26E-07	4.15E-08	2.00E-08
R_{41-42}	−1.78E-06	2.14E-08	3.48E-08				

The inlet molar compositions are CH_4 0.01–H_2O 0.01 (SR) and CO_2 0.01 (DR) with balance N_2. The eigenvectors of only the top three eigenvalues are shown. Bold phase indicates elements of eigenvectors and thus reactions above the threshold that are kept in the reduced microkinetic model.

and WGS. The derivation is reported in detail in Appendix A. The resulting rate equations turn out to be
SR reaction:

$$r_{SR} = \frac{k_{55} c_{CH_4}}{(1 + \frac{k_{56}}{k_{57}} \sqrt{\frac{k_1}{k_2} c_{H_2}})(1 + \sqrt{\frac{k_1}{k_2} c_{H_2}} + \frac{k_{19}}{k_{20}} c_{CO})^2} (1 - \eta_{SR}), \quad (1)$$

DR reaction:

$$r_{DR} = \frac{k_{55} c_{CH_4}}{(1 + \frac{k_{56}}{k_{57}} \sqrt{\frac{k_1}{k_2} c_{H_2}})(1 + \sqrt{\frac{k_1}{k_2} c_{H_2}} + \frac{k_{19}}{k_{20}} c_{CO})^2} (1 - \eta_{DR}), \quad (2)$$

and WGS reaction:

$$r_{WGS} = \frac{k_7 \frac{k_{13}}{k_{14}} c_{H_2O}}{(1 + \sqrt{\frac{k_1}{k_2} c_{H_2}} + \frac{k_{19}}{k_{20}} c_{CO})^2} (1 - \eta_{WGS}), \quad (3)$$

Table 4
Reduced microkinetic model for CH_4 steam and dry reforming on Rh–in UBI-QEP format

No.	Reaction	Sticking coefficient (unitless) or pre-exponentials (s^{-1})	Temperature exponent β	Bond index ϕ	Activation energy dependency and typical estimates at $\theta_H = 0.2$ and $\theta_{CO} = 0.15$ at 700 °C (kcal/mol)
R_1	$H_2 + 2^* \rightarrow 2H^*$	7.73E−01	0.9387	0.50	0.0
R_2	$2H^* \rightarrow H_2 + 2^*$	5.56E+11	−0.4347	0.50	$20.0 - 5.0\theta_H - 7.4\theta_{CO} + f(T)$ {12.3}
R_7	$H_2O^* + {}^* \rightarrow H^* + OH^*$	5.74E+11	0.0281	0.55	$f_{2,f}(\theta_{H_2O}, \theta_H, \theta_{OH}, \theta_{CO}, T)$ {18.6}
R_8	$H^* + OH^* \rightarrow H_2O^* + {}^*$	1.80E+09	1.2972	0.55	$f_{2,b}(\theta_{H_2O}, \theta_H, \theta_{OH}, \theta_{CO}, T)$ {16.3}
R_{13}	$H_2O + {}^* \rightarrow H_2O^*$	7.72E−02	1.4067	0.50	0.0
R_{14}	$H_2O^* \rightarrow H_2O + {}^*$	2.06E+13	−1.8613	0.50	$10.8 - 4.5\theta_{H_2O} + 25.0\theta_{OH} + f(T)$ {7.5}
R_{19}	$CO + {}^* \rightarrow CO^*$	5.00E−01	−2.0000	0.50	0.0
R_{20}	$CO^* \rightarrow CO + {}^*$	5.65E+12	1.9879	0.50	$38.5 - 3.7\theta_H - 15.0\theta_{CO} + f(T)$ {32.8}
R_{21}	$CO_2 + {}^* \rightarrow CO_2^*$	3.67E−01	−2.3294	0.50	0.0
R_{22}	$CO_2^* \rightarrow CO_2 + {}^*$	7.54E+10	2.1831	0.50	$5.2 + f(T)$ {2.8}
R_{29}	$CO_2^* + H^* \rightarrow CO^* + OH^*$	4.00E+14	0.0301	0.70	$f_{3,f}(\theta_{H_2O}, \theta_H, \theta_{OH}, \theta_{CO}, T)$ {5.2}
R_{30}	$CO^* + OH^* \rightarrow CO_2^* + H^*$	3.51E+14	−0.0301	0.70	$f_{3,b}(\theta_{H_2O}, \theta_H, \theta_{OH}, \theta_{CO}, T)$ {19.9}
R_{31}	$COOH^* + {}^* \rightarrow CO^* + OH^*$	1.07E+12	−0.4123	0.50	$f_{2,f}(\theta_{H_2O}, \theta_H, \theta_{OH}, \theta_{CO}, T)$ {7.5}
R_{32}	$CO^* + OH^* \rightarrow COOH^* + {}^*$	9.37E+11	0.4123	0.50	$f_{2,b}(\theta_{H_2O}, \theta_H, \theta_{OH}, \theta_{CO}, T)$ {14.6}
R_{33}	$COOH^* + {}^* \rightarrow CO_2^* + H^*$	1.00E+10	−0.4424	0.50	$f_{2,f}(\theta_H, \theta_{CO}, T)$ {7.6}
R_{34}	$CO_2^* + H^* \rightarrow COOH^* + {}^*$	9.99E+09	0.4424	0.50	$f_{2,b}(\theta_H, \theta_{CO}, T)$ {0.0}
R_{35}	$CO^* + H_2O^* \rightarrow COOH^* + H^*$	3.34E+11	−0.2222	0.50	$f_{3,f}(\theta_{H_2O}, \theta_H, \theta_{OH}, \theta_{CO}, T)$ {19.5}
R_{36}	$COOH^* + OH^* \rightarrow CO^* + H_2O^*$	1.20E+09	0.2223	0.50	$f_{3,b}(\theta_{H_2O}, \theta_H, \theta_{OH}, \theta_{CO}, T)$ {0.0}
R_{39}	$CO_2^* + H_2O^* \rightarrow COOH^* + OH^*$	1.78E+12	−0.1922	0.50	$f_{3,f}(\theta_{H_2O}, \theta_{OH}, T)$ {13.1}
R_{40}	$COOH^* + OH^* \rightarrow CO_2^* + H_2O^*$	5.60E+09	0.1922	0.50	$f_{3,b}(\theta_{H_2O}, \theta_{OH}, T)$ {18.3}
R_{55}	$CH_4 + 2^* \rightarrow CH_3^* + H^*$	5.72E−01	0.7883	0.50	$f_{1,f}(\theta_H, \theta_{CO}, T)$ {14.7}
R_{56}	$CH_3^* + H^* \rightarrow CH_4 + 2^*$	7.72E+10	−0.7883	0.50	$f_{1,b}(\theta_H, \theta_{CO}, T)$ {5.5}
R_{57}	$CH_3^* + {}^* \rightarrow CH_2^* + H^*$	2.49E+10	0.0862	0.50	$f_{2,f}(\theta_H, \theta_{CO}, T)$ {12.2}
R_{58}	$CH_2^* + H^* \rightarrow CH_3^* + {}^*$	2.57E+09	−0.0862	0.50	$f_{2,b}(\theta_H, \theta_{CO}, T)$ {25.7}
R_{59}	$CH_2^* + {}^* \rightarrow CH^* + H^*$	5.50E+10	−0.1312	0.50	$f_{2,f}(\theta_H, \theta_{CO}, T)$ {21.7}
R_{60}	$CH^* + H^* \rightarrow CH_2^* + {}^*$	7.27E+09	0.1312	0.50	$f_{2,b}(\theta_H, \theta_{CO}, T)$ {20.6}
R_{61}	$CH^* + {}^* \rightarrow C^* + H^*$	4.58E+12	−0.2464	0.50	$f_{2,f}(\theta_H, \theta_{CO}, T)$ {28.9}
R_{62}	$C^* + H^* \rightarrow CH^* + {}^*$	2.18E+11	0.2464	0.50	$f_{2,b}(\theta_H, \theta_{CO}, T)$ {14.1}
R_{63}	$CH_3^* + O^* \rightarrow CH_2^* + OH^*$	2.96E+11	−0.1906	0.50	$f_{3,f}(\theta_{H_2O}, \theta_{OH}, T)$ {6.7}
R_{64}	$CH_2^* + OH^* \rightarrow CH_3^* + O^*$	3.38E+10	0.1906	0.50	$f_{3,b}(\theta_{H_2O}, \theta_{OH}, T)$ {34.5}
R_{69}	$CH_2^* + H_2O^* \rightarrow CH_3^* + OH^*$	5.73E+10	−0.7208	0.50	$f_{3,f}(\theta_{H_2O}, \theta_{OH}, T)$ {20.3}
R_{70}	$CH_3^* + OH^* \rightarrow CH_2^* + H_2O^*$	1.74E+09	0.7208	0.50	$f_{3,b}(\theta_{H_2O}, \theta_{OH}, T)$ {4.4}
R_{71}	$CH^* + H_2O^* \rightarrow CH_2^* + OH^*$	6.49E+11	−0.5033	0.50	$f_{3,f}(\theta_{H_2O}, \theta_{OH}, T)$ {21.2}
R_{72}	$CH_2^* + OH^* \rightarrow CH^* + H_2O^*$	1.54E+10	0.5033	0.50	$f_{3,b}(\theta_{H_2O}, \theta_{OH}, T)$ {19.9}
R_{73}	$C^* + H_2O^* \rightarrow CH^* + OH^*$	9.74E+11	−0.3882	0.50	$f_{3,f}(\theta_{H_2O}, \theta_{OH}, T)$ {17.0}
R_{74}	$CH^* + OH^* \rightarrow C^* + H_2O^*$	6.41E+10	0.3882	0.50	$f_{3,b}(\theta_{H_2O}, \theta_{OH}, T)$ {29.3}
R_{79}	$CO^* + H^* \rightarrow C^* + OH^*$	1.18E+12	0.2944	0.15	$f_{3,f}(\theta_{H_2O}, \theta_H, \theta_{OH}, \theta_{CO}, T)$ {22.6}
R_{80}	$C^* + OH^* \rightarrow CO^* + H^*$	7.60E+12	−0.2944	0.15	$f_{3,b}(\theta_{H_2O}, \theta_H, \theta_{OH}, \theta_{CO}, T)$ {0.0}

The reaction rate constant (k) is calculated as follows:

$$k = \frac{A}{\Gamma_{Rh}^{n-1}}\left(\frac{T}{T_0}\right)^{\beta} e^{-E/RT} \quad \text{or } k = \frac{s}{\Gamma_{Rh}^{n}}\sqrt{\frac{RT}{2\pi MW}}\left(\frac{T}{T_0}\right)^{\beta} e^{-E/RT},$$

where A is the pre-exponential, s is the sticking coefficient, Γ_{Rh} is the site density, n is the reaction order, E is the activation energy, R is the ideal gas constant and T_0 is the reference temperature (300 K). Activation energies are calculated according to the UBI-QEP framework [26] and the expressions are given in Table 6. In the simulations, Γ_{Rh} has been set equal to 2.49×10^{-9} mol/cm^2.

The ith elementary-like reaction rate is calculated according to:

$$r_i = k_i \prod_{j=1}^{K_{tot}} X_j^{\nu_{i,j}} = k_i \Gamma_{Rh}^{n} \prod_{j=1}^{K_{surf}} \theta_j^{\nu_{i,j}} \quad \text{for surface reaction}$$

or

$$r_i = k_i \prod_{j=1}^{K_{tot}} X_j^{\nu_{i,j}} = k_i \Gamma_{Rh}^{n} X_{\text{gas species}}^{\nu_i} \prod_{j=1}^{K_{surf}} \theta_j^{\nu_{i,j}} \quad \text{for adsorption reaction.}$$

Here X_j is the mole concentration either of gas species (mol/cm^3) or adspecies (mol/cm^2); θ_j is the site fraction; r_i is the rate of the ith reaction (mol/cm^2/s).

Table 5
Heats of chemisorption [16,21,22]

Surface species	Heat of chemisorption, Q (kcal/mol)	Temperature dependence [42] $(Q(T_0) - Q(T))/R\Delta T$
H^*	$62.3 - 2.5\theta_H - 3.7\theta_{CO}$	1.5
OH^*	$70.0 - 33\theta_O + 25\theta_{H_2O}$	2.0
H_2O^*	$10.8 - 4.5\theta_{H_2O} + 25\theta_{OH}$	2.5
CO^*	$38.5 - 15.0\theta_{CO} - 3.7\theta_H$	2.0
CO_2^*	159.0	2.0
C^*	69.2	1.5
CH^*	151.2	2.0
CH_2^*	109.3	2.5
CH_3^*	42.4	2.5
CH_4	6.0	2.0

where η is the equilibrium factor defined for SR (and similarly for DR and WGS) as

$$\eta_{SR} = \frac{K_{SR}}{K_{\text{equilibrium,SR}}}, \tag{4}$$

$$K_{SR} = \frac{p_{CO}\, p_{H_2}^3}{p_{CH_4}\, p_{H_2O}}, \tag{5}$$

and

$$K_{\text{equilibrium,SR}} = \exp\left(-\frac{\Delta G_{SR}^0(T)}{RT}\right). \tag{6}$$

In Eq. (5), an ideal mixture and gas behavior are assumed. Moreover, a reference pressure of 1 bar was considered. This must be

consistent with ΔG^0_{SR} in Eq. (6). Eqs. (1) and (3) or (2) and (3) are the rates needed to model SR or DR, respectively.

On the basis of this analysis and consistent with the foregoing discussion, the rate expressions for SR and DR (far from equilibrium) have the same reaction orders with respect to reactants and products. Yet, in principle the reaction rate could be different for SR and DR, due to the different coverages in the reaction constants k_i, but these effects turned out to be minor, as discussed earlier. Note that reduced rate expressions always hold under certain conditions, and that large extrapolations may lead to inaccurate predictions. For example, both the SR and DR rates do not apply in the limit of complete lack of the co-reactant. As elaborated in the appendix, the rate of the WGS reaction is faster than the full model, but this is unimportant, because this reaction is close to equilibrium under typical SR and DR conditions.

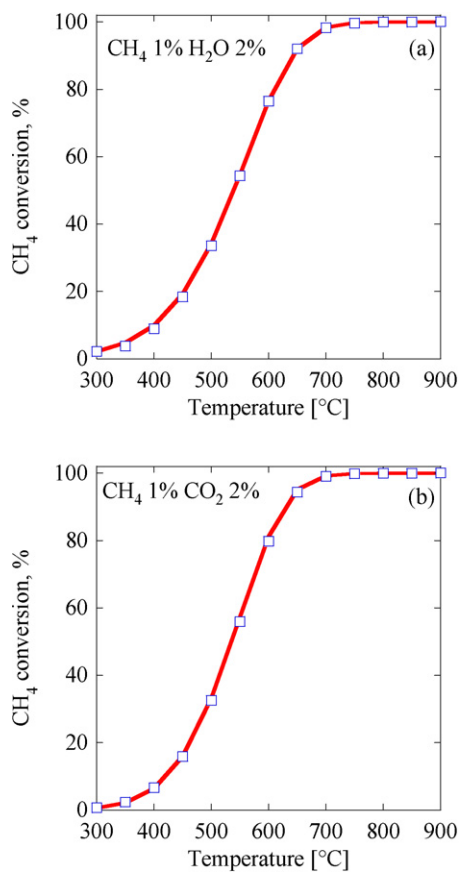

Fig. 9. Comparison of the full microkinetic model (lines) and the 2-step reduced model with UBI-QEP estimated parameters (symbols). Operating conditions are those of Fig. 2.

3.2.1. Assessment of the overall reaction rate expressions

In the foregoing expressions, the activation energies are calculated according to the UBI-QEP theory [26]. According to this theory, activation energies of the surface reaction depend on heats chemisorption of the involved species, given in Table 5. A summary of the expressions used for activation energy calculation is given in Table 6. Because the heats of chemisorption of ad-species usually are coverage-dependent (Table 5), activation energies also are coverage-dependent, and the MARI surface coverages should be solved for using the following equations (see Appendix A for derivation):

$$\theta_H = \frac{\sqrt{\frac{k_1}{k_2} c_{H_2}}}{1 + \sqrt{\frac{k_1}{k_2} c_{H_2}} + \frac{k_{19}}{k_{20}} c_{CO}} \tag{7}$$

and

$$\theta_{CO} = \frac{\frac{k_{19}}{k_{20}} c_{CO}}{1 + \sqrt{\frac{k_1}{k_2} c_{H_2}} + \frac{k_{19}}{k_{20}} c_{CO}}. \tag{8}$$

Fig. 9 compares the two-step reduced model with the full microkinetic model for the operating conditions used in the derivation. (Comparison of full model to data was done earlier and is not repeated here.) The predictions of the two-step reduced model and the full microkinetic model (82 reactions; UBI-QEP theory) are in good agreement. Equations (1) and (2) [along with Eq. (3)] were developed at a particular set of operating. To exploit the validity of the reaction rate expression, we performed a "diversity test," comparing the prediction using the two-step reduced model and the full microkinetic model for nondiluted conditions and different values of H_2O/CH_4 or CO_2/CH_4 ratios. Fig. 10 compares results for nondiluted conditions and three values of the co-reactant/CH_4 ratio. Overall, the two-step reduced model captures the full model fairly well over the entire range of conditions investigated.

To simplify calculations, the UBI-QEP–based activation energies were fitted as linear functions of coverages. Then, substituting those expressions in Eqs. (1)–(3), effective reaction parameters were determined from the full microkinetic model, rather than from fitting them to experimental data. The final expressions are reported in Table 7. Fig. 2 compares model predictions of the reduced two-step model with these approximate activation energies (dashed lines), the full microkinetic (solid line), and the experimental data (symbols); only moderate deviations between the full model and the two-step model are seen. (These deviations are due to the approximation of the UBI-QEP values with a Chemkin-compatible format.) Overall, without using UBI-QEP equations in the two-step model, the agreement is satisfactory.

Table 6
Summary of equations for computing activation energies of surface reactions according to UBI-QEP framework [26]

Reaction type	Activation energy	Notes
$AB + 2^* \rightarrow A^* + B^*$ (dissociative adsorption)	$E_f = \phi[\Delta H_{surf,f} - Q_{AB} + \frac{Q_A Q_B}{Q_A + Q_B}]$	$\Delta H_{surf,f} = D_{AB} - Q_A - Q_B$ $D_{AB} = H_A + H_B - H_{AB}$
$AB^* + * \rightarrow A^* + B^*$ (dissociation reaction)	$E_f = \phi[\Delta H_{surf,f} + \frac{Q_A Q_B}{Q_A + Q_B}]$	$\Delta H_{surf,f} = D_{AB} - Q_A - Q_B$ $D_{AB} = H_A + H_B - H_{AB}$
$A^* + B^* \rightarrow C^* + D^*$ (disproportionation reaction)	$E_f = \phi[\Delta H_{surf,f} + \frac{Q_C Q_D}{Q_C + Q_D}]$	$\Delta H_{surf,f} = \Delta H_{gas,f} + Q_A + Q_B - Q_C - Q_D$ $D_{AB} = H_C + H_D - H_A - H_B$

For all reactions, the backward activation energy is $E_b = E_f - \Delta H_{surf,f}$. If either E_f or E_b becomes negative, it is set to zero and the other one equal to the heat of reaction. The dependence of heats of chemisorption on coverage and temperature is given in Table 5. H_i is the gas-phase enthalpy of the ith species, D is the gas-phase dissociation energy, ϕ is the bond index ($0 < \phi < 1$).

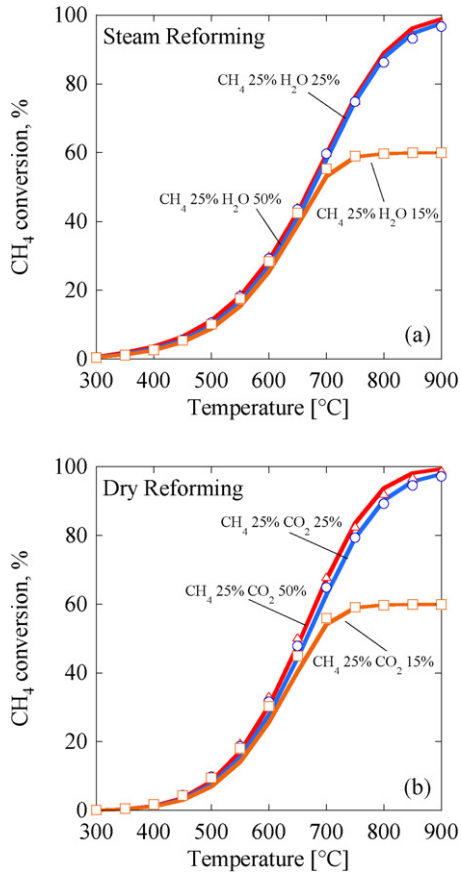

Fig. 10. Diversity test for the 2-step reduced model (symbols) vs the full microkinetic model (lines) for co-reactant/CH_4 ratios indicated for (a) SR and (b) DR.

Table 7
Overall rate expressions for methane steam and dry reforming and for water–gas shift reactions on Rh

Reaction	Rate expression
SR $CH_4 + H_2O \rightarrow CO + 3H_2$	$r_{SR} = \frac{\gamma_4 c_{CH_4}}{(1+\gamma_1\sqrt{c_{H_2}})(1+\gamma_2\sqrt{c_{H_2}}+\gamma_3 c_{CO})^2}(1-\eta_{SR})$
DR $CH_4 + CO_2 \rightarrow 2CO + 2H_2$	$r_{DR} = \frac{\gamma_4 c_{CH_4}}{(1+\gamma_1\sqrt{c_{H_2}})(1+\gamma_2\sqrt{c_{H_2}}+\gamma_3 c_{CO})^2}(1-\eta_{DR})$
WGS $CO + H_2O \rightarrow CO_2 + H_2$	$r_{WGS} = \frac{\gamma_5 c_{H_2O}}{(1+\gamma_2\sqrt{c_{H_2}}+\gamma_3 c_{CO})^2}(1-\eta_{WGS})$

Reaction rates are in mol/cm^2/s, concentrations c_i are in mol/cm^3. Parameters γ_i are calculated according to the following expressions:

$$\gamma_1 = 3.37162 \times 10^{-1} T^{0.6706} \exp\left(\frac{5892.67 - 513.28\theta_H - 232.49\theta_{CO}}{T}\right),$$

$$\gamma_2 = 2.7564607 \times 10^{1} T^{-0.2997} \exp\left(\frac{5032.17 - 1258.04\theta_H - 1861.90\theta_{CO}}{T}\right),$$

$$\gamma_3 = 1.0510 \times 10^{11} T^{-4.6} \exp\left(\frac{19288.30 - 1861.90\theta_H - 7548.25\theta_{CO}}{T}\right),$$

$$\gamma_4 = 1.7736 \times 10^{5} T^{-0.522} \exp\left(-\frac{5137.84 + 528.38\theta_H + 779.99\theta_{CO}}{T}\right),$$

$$\gamma_5 = 6.7694 \times 10^{-4} T^{+1.887} \exp\left(-\frac{3270.91 + 508.25\theta_H + 754.83\theta_{CO}}{T}\right).$$

WGS always occurs at equilibrium along with SR and DR. The coverages can be calculated solving at each step the following implicit expressions:

$$\theta_{CO} = \frac{\gamma_3 c_{CO}}{1 + \gamma_2\sqrt{c_{H_2}} + \gamma_3 c_{CO}},$$

$$\theta_H = \frac{\gamma_2\sqrt{c_{H_2}}}{1 + \gamma_2\sqrt{c_{H_2}} + \gamma_3 c_{CO}}.$$

When using the WGS expression in DR, a small fraction of water (e.g., 1×10^{-8} v/v) must be included in the feed stream.

4. Effective reaction order analysis for SR, DR, and WGS forward rate

In this section, we explore the reaction orders in the reduced rate expression for SR, DR, and WGS with respect to CH_4, H_2O, H_2, and CO. The rate expression for SR and DR is first order with respect to CH_4 and zeroth order with respect to the co-reactant. This behavior is expected, because the RDS is the methane dehydrogenation and the co-reactant activation is in partial equilibrium, as reported in Fig. 3.

Our expressions show a potentially inhibiting effect with respect to both CO and H_2. It is worth understanding the trend of the denominator of Eq. (1) for different values of product co-feeding, to assess the magnitude of product inhibition and its trend with temperature. For temperatures below 550 °C, considerable inhibition by CO and H_2 occurs, whereas with increasing temperature, the product inhibition decreases due to faster desorption. For temperatures above 700 °C, the CO inhibition becomes negligible, whereas H* still blocks sites even at higher temperatures for H_2 partial pressures >10 kPa (100 kPa total pressure). Wei and Iglesia [36] reported that products have no effect on the forward reaction rate for SR or DR based on experiments conducted at 550–750 °C at very low reactant conversions. Under such conditions, our reduced expressions show a negligible effect of CO (especially for temperatures above 600 °C), whereas H* blocks sites even at 800 °C. The difference in the temperature above which products are not inhibited can be ascribed to, among other factors, uncertainties in model parameters, such as the heat of chemisorption of H_2 and CO, as discussed previously [21,22]. Equations (1) and (2) account for product inhibition especially at lower temperatures, in line with previous experimental findings [18]. Product inhibition becomes negligible at higher temperatures; thus, the effective reaction order with respect to the products changes with temperature.

Concerning the WGS reaction, the model suggests a rate expression that is first order with respect to H_2O and zeroth order with respect to CO at sufficiently high temperatures, where blocking by CO* is negligible. The same reaction orders have been inferred experimentally by Donazzi et al. [23].

5. Conclusion

Methane SR and DR on Rh were analyzed using a comprehensive and thermodynamically consistent microkinetic model. Our analysis demonstrated the mechanistic analogies between the two processes. In particular, regardless of the co-reactant used, methane consumption ($CH_4 \rightarrow C^* \rightarrow CO^*$) is due to pyrolysis and carbon oxidation by OH*. The role of the co-reactant (either CO_2 or H_2O) is to provide the main oxidizer, OH*. Moreover, in line with isotopic kinetic experiments reported previously, methane activation is predicted to be the RDS, and all of the steps involving the co-reactant are quasi-equilibrated; consequently, in both SR and DR, methane activation is the sole kinetically relevant step. It also was found that SR and DR always occur with the WGS reaction close to equilibrium. Moreover, we have proposed a hierarchy of models for SR and DR, including a reduced microkinetic model and the first fundamentally derived (based on a detailed model) two-step rate expression model. These overall rate equations are not based on an assumed mechanism with effective parameters fitted to experimental data; rather, the parameters are related to the rate constants of the elementary-like reactions of the microkinetic model. Overall, our kinetic analysis is able to correctly predict the most important features found in experiments, namely that the overall reaction rate exhibits a first order dependence on CH_4

concentration but is independent of the co-reactant (H_2O or CO_2). Product inhibition, which becomes important at lower temperatures, also is predicted.

Acknowledgments

Financial support was provided by MIUR-Rome (PRIN 2006). The wok of D.G.V. was supported in part by the National Science Foundation (CBET-0729701).

Appendix A. Derivation of the global rate equations

A.1. Steam reforming

The steady-state balance equations for the surface species according to the reduced microkinetic model reported in Table 4 are

$$\frac{d\theta_H}{dt} = 2r_1 - 2r_2 + r_7 - r_8 - r_{29} + r_{30} + r_{33} - r_{34} + r_{35} - r_{36} + r_{55} - r_{56} + r_{57} - r_{58} + r_{59} - r_{60} + r_{61} - r_{62} - r_{79} + r_{80} = 0, \tag{9}$$

$$\frac{d\theta_{OH}}{dt} = r_7 - r_8 + r_{29} - r_{30} + r_{31} - r_{32} + r_{39} - r_{40} + r_{69} - r_{70} + r_{71} - r_{72} + r_{79} - r_{80} = 0, \tag{10}$$

$$\frac{d\theta_{H_2O}}{dt} = -r_7 + r_8 + r_{13} - r_{14} - r_{35} + r_{36} - r_{39} + r_{40} - r_{69} + r_{70} - r_{71} + r_{72} = 0, \tag{11}$$

$$\frac{d\theta_{CO}}{dt} = r_{19} - r_{20} + r_{29} - r_{30} + r_{31} - r_{32} - r_{35} + r_{36} - r_{79} + r_{80} = 0, \tag{12}$$

$$\frac{d\theta_{CO_2}}{dt} = r_{21} - r_{22} - r_{29} + r_{30} + r_{33} - r_{34} - r_{39} + r_{40} = 0, \tag{13}$$

$$\frac{d\theta_{COOH}}{dt} = -r_{31} + r_{32} - r_{33} + r_{34} + r_{35} - r_{36} + r_{39} - r_{40} = 0, \tag{14}$$

$$\frac{d\theta_C}{dt} = r_{61} - r_{62} + r_{79} - r_{80} = 0, \tag{15}$$

$$\frac{d\theta_{CH}}{dt} = r_{59} - r_{60} - r_{61} + r_{62} - r_{71} + r_{72} = 0, \tag{16}$$

$$\frac{d\theta_{CH_2}}{dt} = r_{57} - r_{58} - r_{59} + r_{60} - r_{69} + r_{70} + r_{71} - r_{72} = 0, \tag{17}$$

$$\frac{d\theta_{CH_3}}{dt} = r_{55} - r_{56} - r_{57} + r_{58} + r_{69} - r_{70} = 0, \tag{18}$$

$$\theta_H + \theta_{OH} + \theta_{H_2O} + \theta_{CO} + \theta_{CO_2} + \theta_{COOH} + \theta_C + \theta_{CH} + \theta_{CH_2} + \theta_{CH_3} + \theta_{Rh} = 1. \tag{19}$$

All the adsorption/desorption steps of reactants and products, with the exception of CH_4, are in PE (see Fig. 4). Then it follows that

$$r_1 = r_2, \tag{20}$$

$$r_{13} = r_{14}, \tag{21}$$

$$r_{19} = r_{20}, \tag{22}$$

$$r_{21} = r_{22}. \tag{23}$$

From Eqs. (20)–(23), the coverages of H_2, H_2O, CO, and CO_2 are derived as follows:

$$\theta_H = \sqrt{\frac{k_1}{k_2} c_{H_2}}\,\theta_{Rh} = \alpha_H \theta_{Rh}, \tag{24}$$

$$\theta_{H_2O} = \frac{k_{13}}{k_{14}} c_{H_2O}\theta_{Rh} = \alpha_{H_2O}\theta_{Rh}, \tag{25}$$

$$\theta_{CO} = \frac{k_{19}}{k_{20}} c_{CO}\theta_{Rh} = \alpha_{CO}\theta_{Rh}, \tag{26}$$

$$\theta_{CO_2} = \frac{k_{21}}{k_{22}} c_{CO_2}\theta_{Rh} = \alpha_{CO_2}\theta_{Rh}. \tag{27}$$

Comparing the terms in Eq. (18) and adopting a threshold value of 1% (i.e., omitting terms whose magnitude [in absolute value] is <1% of the highest in each equation), Eq. (18) can be simplified as follows:

$$\frac{d\theta_{CH_3}}{dt} = r_{55} - r_{56} - r_{57} = 0, \tag{28}$$

and the coverage of CH_3^* (at steady state) turns out to be

$$\theta_{CH_3} = \left(\frac{k_{55}c_{CH_4}}{k_{56}\alpha_H + k_{57}}\right)\theta_{Rh} = \alpha_{CH_3}\theta_{Rh}. \tag{29}$$

As already discussed, Figs. 8a and 8b show the steady-state coverage axial profiles for SR at 400 and 600 °C, respectively. From these profiles, it is clear that the dominant species are H^* and CO^*. Consequently, Eq. (19) can be simplified as

$$\theta_H + \theta_{CO} + \theta_{Rh} = 1. \tag{30}$$

Substituting Eqs. (24) and (26), an expression for the vacancies is derived,

$$\theta_{Rh} = \frac{1}{1 + \sqrt{\frac{k_1}{k_2}c_{H_2}} + \frac{k_{19}}{k_{20}}c_{CO}}. \tag{31}$$

Because CH_3^* dehydrogenation is the RDS, the forward reaction rate for the SR reaction turns out to be

$$r_{SR,forward} = r_{57} = \frac{k_{55}c_{CH_4}}{(1 + \frac{k_{56}}{k_{57}}\sqrt{\frac{k_1}{k_2}c_{H_2}})(1 + \sqrt{\frac{k_1}{k_2}c_{H_2}} + \frac{k_{19}}{k_{20}}c_{CO})^2}. \tag{32}$$

To account for the equilibrium, the factor η_{SR} is used. The resulting rate expression for the reversible reaction rate is

$$r_{SR} = \frac{k_{55}c_{CH_4}}{(1 + \frac{k_{56}}{k_{57}}\sqrt{\frac{k_1}{k_2}c_{H_2}})(1 + \sqrt{\frac{k_1}{k_2}c_{H_2}} + \frac{k_{19}}{k_{20}}c_{CO})^2}(1 - \eta_{SR}). \tag{33}$$

A.2. Dry reforming reaction

Equations (24)–(30) remain valid also for DR. Given that RDS is the same as for SR, following the same steps reported for the SR model reduction, the reversible rate expression for DR turns out to be

$$r_{DR} = \frac{k_{55}c_{CH_4}}{(1 + \frac{k_{56}}{k_{57}}\sqrt{\frac{k_1}{k_2}c_{H_2}})(1 + \sqrt{\frac{k_1}{k_2}c_{H_2}} + \frac{k_{19}}{k_{20}}c_{CO})^2}(1 - \eta_{DR}). \tag{34}$$

A.3. Water–gas shift reaction

In what follows, we derive a rate expression for the WGS reaction. At typical temperatures of SR or DR, η_{WGS} is nearly 1 for all operating conditions investigated herein (data not shown). The fact that WGS reaction is quasi-equilibrated is in agreement with the observations of Wei and Iglesia [36]. The WGS reaction changes the local composition along a reactor and, in conjunction with the SR or DR reaction, controls the fractions of products. The SR or DR process can be modeled using the rate from Eq. (1) or (2) along with the relation $\eta_{WGS} = 1$. Alternatively, a rate equation could be used for the WGS reaction. Deriving a rate expression for the WGS requires conditions in which the reaction is far from equilibrium to identify a RDS. Thus, we performed SA for the WGS reaction ($CO + H_2O$) for such conditions. The results (not shown) indicate that the RDS for the WGS reaction is

$H_2O^* + {}^* \rightarrow OH^* + H^*$ (R_7).

At low temperatures, along with coverages of H^* and CO^*, the coverage of CH^* also is high. To simplify the derivation, we used Eqs. (24)–(27) for the WGS reaction without modification. Then, the forward reaction rate for WGS is

$$r_{\mathrm{WGS,forward}} = \frac{k_7 \frac{k_{13}}{k_{14}} c_{\mathrm{H_2O}}}{(1 + \sqrt{\frac{k_1}{k_2} c_{\mathrm{H_2}}} + \frac{k_{19}}{k_{20}} c_{\mathrm{CO}})^2}. \tag{36}$$

A reversible expression is obtained by including the ratio η_{WGS}, as follows:

$$r_{\mathrm{WGS}} = \frac{k_7 \frac{k_{13}}{k_{14}} c_{\mathrm{H_2O}}}{(1 + \sqrt{\frac{k_1}{k_2} c_{\mathrm{H_2}}} + \frac{k_{19}}{k_{20}} c_{\mathrm{CO}})^2} (1 - \eta_{\mathrm{WGS}}). \tag{37}$$

Notation

a_v	Specific surface per unit volume, cm^{-1}
a_{Rh}	Specific Rh surface per unit volume, cm^{-1}
c_i	Species concentration, $\mathrm{mol/cm}^3$
d_h	Hydraulic diameter, cm
D_i	Species diffusivity, cm^2/s
k_i	Reaction constant, reaction specific
$k_{\mathrm{mat},i}$	Mass transfer coefficient, cm/s
MW_i	Molar mass, g/mol
Q	Heat of chemisorption, kcal/mol
p_i	Partial pressure, Pa
r	Reaction rate, $\mathrm{mol/cm}^2/\mathrm{s}$
R_{gas}	Universal gas constant, kcal/mol/K
Sh	Sherwood number
T	Temperature, K
z	Reactor axial length, cm
V	Reactor volume, cm^3
W_i	Mass flux, g/s

Greek letters

Γ	Site density, $\mathrm{mol/cm}^2$
η	Equilibrium ratio, K_p/K_{eq}, dimensionless
θ	Coverage site fraction, dimensionless
ν	Stoichiometric coefficient
ρ	Gas density, $\mathrm{g/cm}^3$
φ	Partial equilibrium index, $\frac{r_f}{r_f + r_b}$
ω	Mass fraction, dimensionless

Abbreviations

MARI	Most Abundant Reactive Intermediate
PCA	Principal Component Analysis
PE	Partial Equilibrium
POX	Partial Oxidation
RDS	Rate Determining Step
SA	Sensitivity Analysis
SR	Steam Reforming
DR	Dry Reforming
WGS	Water–Gas Shift

References

[1] G. Mulder, J. Hetland, G. Lenaers, Int. J. Hydrogen Energy 32 (2007) 1324–1331.
[2] NRC, The Hydrogen Economy: Opportunities, Costs, Barriers and R&D Needs, The National Academies Press, Washington, DC, 2004.
[3] T. Rostrup-Nielsen, Catal. Today 106 (2005) 293–296.
[4] J.R. Rostrup-Nielsen, Catal. Today 71 (2002) 243–247.
[5] J.A. Moulijn, M. Makkee, A. Van Diepen, Chemical Process Technology, New York, 2001.
[6] D.O.E.-. USA. Hydrogen, Fuel Cells and Infrastructure Technologies Program. 2008, Available from: http://www1.eere.energy.gov/hydrogenandfuelcells/production/natural_gas.html.
[7] D.A. Hickman, L.D. Schmidt, Science 259 (1993) 343–346.
[8] I. Tavazzi, M. Maestri, A. Beretta, G. Groppi, E. Tronconi, P. Forzatti, AIChE J. 52 (2006) 3234–3245.
[9] T.V. Choudhary, V.R. Choudhary, Angew. Chem. Int. Ed. 47 (2008) 1828–1847.
[10] A.A. Gokhale, S. Kandoi, J.P. Greeley, M. Mavrikakis, J.A. Dumesic, Chem. Eng. Sci. 59 (2004) 4679–4691.
[11] J.A. Dumesic, D.F. Rudd, L.M. Aparicio, J.E. Rekoske, A.A. Trevino, The Microkinetics of Heterogeneous Catalysis, American Chemical Society, Washington, DC, 1993.
[12] M. Maestri, A. Beretta, G. Groppi, E. Tronconi, D.G. Vlachos, Chem. Eng. Sci. 63 (2008) 2657–2669.
[13] S. Raimondeau, D.G. Vlachos, Chem. Eng. J. 90 (2002) 3–23.
[14] S.R. Deshmukh, A.B. Mhadeshwar, M.I. Lebedeva, D.G. Vlachos, Int. J. Multiscale Comput. Eng. 2 (2004) 221–238.
[15] D.A. Hickman, L.D. Schmidt, AIChE J. 39 (1993) 1164–1177.
[16] A.B. Mhadeshwar, D.G. Vlachos, J. Phys. Chem. B 109 (2005) 16819–16835.
[17] R. Schwiedernoch, S. Tischer, C. Correa, O. Deutschmann, Chem. Eng. Sci. 58 (2003) 633–642.
[18] A. Donazzi, A. Beretta, G. Groppi, P. Forzatti, J. Catal. 255 (2008) 241–258.
[19] I. Tavazzi, A. Beretta, G. Groppi, P. Forzatti, J. Catal. 241 (2006) 1–13.
[20] A.L.Y. Tonkovich, B. Yang, S.T. Perry, S.P. Fitzgerald, Y. Wang, Catal. Today 120 (2007) 21–29.
[21] M. Maestri, D.G. Vlachos, A. Beretta, G. Groppi, E. Tronconi, AIChE J., (2008) submitted for publication.
[22] M. Maestri, Short-Contact-Time Catalytic Partial Oxidation of Methane on Rh: Reactor Analysis and Microkinetic Modeling. Ph.D. thesis, Politecnico di Milano, Milano, 2008.
[23] A. Donazzi, A. Beretta, G. Groppi, P. Forzatti, J. Catal. 255 (2008) 259–268.
[24] P. Aghalayam, Y.K. Park, D.G. Vlachos, AIChE J. 46 (2000) 2017–2029.
[25] D.G. Vlachos, A.B. Mhadeshwar, N.S. Kaisare, Comput. Chem. Eng. 30 (2006) 1712–1724.
[26] E. Shustorovich, H. Sellers, Surf. Sci. Rep. 31 (1998) 5–119.
[27] E. Shustorovich, Russ. J. Phys. Chem. B 1 (2007) 307–329.
[28] O. Hougen, K. Watson, Chemical Processes Principles: Kinetics and Catalysis, Wiley, London, 1947.
[29] S.R. Deshmukh, A.B. Mhadeshwar, D.G. Vlachos, Indust. Eng. Chem. Res. 43 (2004) 2986–2999.
[30] A.B. Mhadeshwar, D.G. Vlachos, Catal. Today 105 (2005) 162–172.
[31] S.R. Deshmukh, D.G. Vlachos, Combust. Flame 149 (2007) 366–383.
[32] A. Beretta, P. Baiardi, D. Prina, P. Forzatti, Chem. Eng. Sci. 54 (1999) 765–773.
[33] P. Aghalayam, Y.K. Park, N. Fernandes, V. Papavassiliou, A.B. Mhadeshwar, D.G. Vlachos, J. Catal. 213 (2003) 23–38.
[34] J.A. Dumesic, J. Catal. 185 (1999) 496–505.
[35] A.M. Efstathiou, A. Kladi, V.A. Tsipouriari, X.E. Verykios, J. Catal. 158 (1996) 64–75.
[36] J.M. Wei, E. Iglesia, J. Catal. 225 (2004) 116–127.
[37] A. Erdohelyi, J. Cserenyi, F. Solymosi, J. Catal. 141 (1993) 287–299.
[38] M.C.J. Bradford, M.A. Vannice, Appl. Catal. A 142 (1996) 73–96.
[39] S. Vajda, T. Turanyi, J. Phys. Chem. 90 (1986) 1664–1670.
[40] S. Vajda, P. Valko, T. Turanyi, Int. J. Chem. Kinet. 17 (1985) 55–81.
[41] J.R. Rostrup-Nielsen, J.H.B. Hansen, J. Catal. 144 (1993) 38–49.
[42] A.B. Mhadeshwar, H. Wang, D.G. Vlachos, J. Phys. Chem. B 107 (2003) 12721–12733.